This article has been accepted for publication in IEEE Transactions on Robotics. This is the author's version which has not been fully edited and content may change prior to final publication. Citation information: DOI 10.1109/TRO.2025.3526087

Design, Modeling, and Optimization of Hydraulically Powered Double-Joint Soft Robotic Fish

Sijia Liu, Chunbao Liu, Guowu Wei, *Member, IEEE*, Luquan Ren, and Lei Ren, *Member, IEEE*

Abstract—This paper explores a hydraulically powered double-joint soft robotic fish called HyperTuna and a set of locomotion optimization methods. HyperTuna has an innovative, highly efficient actuation structure that includes a four-cylinder piston pump and a double-joint soft actuator with self-sensing. We conducted deformation analysis on the actuator and established a finite element model to predict its performance. A closed-loop strategy combining a central pattern generator controller and a proportional–integral–derivative controller was developed to control the swimming posture accurately. Next, a dynamic model for the robotic fish was established considering the soft actuator, and the model parameters were identified via data-driven methods. Then, a particle swarm optimization algorithm was adopted to optimize the control parameters and improve the locomotion performance. Experimental results showed that the maximum speed increased by 3.6% and the cost of transport (COT) decreased by up to 13.9% at 0.4 m/s after optimization. The proposed robotic fish achieved a maximum speed of 1.12 BL/s and a minimum COT of 12.1 J/(kg·m), which are outstanding relative to those of similar soft robotic fish. Lastly, HyperTuna completed turning and diving–floating movements and long-distance continuous swimming in open water, which confirmed its potential for practical application.

***Index Terms*—Robotic fish, hydraulically powered, soft actuator, particle swarm optimization.**

This work was supported in part by the Projects of National Natural Science Foundation of China under Grants 52075216, 91948302, and 91848204, in part by the Fundamental Research Funds for the Central Universities, Jilin University under Grant 2022-JCXK-15, and in part by Jilin Scientific and Technological Development Program under Grant 3D5224054428. (Corresponding author: Chunbao Liu.)

Sijia Liu is with the School of Mechanical and Aerospace Engineering, Jilin University, Changchun 130022, China (e-mail: liusj21@mails.jlu.edu.cn).

Chunbao Liu is with the School of Mechanical and Aerospace Engineering, Jilin University, Changchun 130022, China, and also with the Key Laboratory of CNC Equipment Reliability Ministry of Education, Jilin University, Changchun 130000, China (e-mail: liuchunbao@jlu.edu.cn).

Guowu Wei is with the School of Science, Engineering, and Environment, University of Salford, M5 4WT Salford, U.K. (e-mail: g.wei@salford.ac.uk).

Luquan Ren is with the Key Laboratory of Bionic Engineering, Ministry of Education, Jilin University, Changchun 130022, China, with the Weihai Institute for Bionics, Jilin University, Weihai, China (e-mail: lqren@jlu.edu.cn)

Lei Ren is with the Key Laboratory of Bionic Engineering, Ministry of Education, Jilin University, Changchun 130022, China, and also with the School of Mechanical, Aerospace and Civil Engineering, University of Manchester, M13 9PL Manchester, U.K. (e-mail: lren@jlu.edu.cn).

Color versions of one or more of the figures in this article are available online at http://ieeexplore.ieee.org

I. INTRODUCTION

Natural selection, over millions of years, has bestowed fish with almost perfect body structures [1]. Their functional design includes a flexible body performing undulatory motion [2] and numerous control surfaces [3], [4] that enable them to maneuver rapidly in underwater environments. Their remarkable locomotion abilities have driven researchers to design man-made systems that interact with aquatic environments efficiently, especially autonomous underwater vehicles.

In recent years, researchers have designed many mechanical structures to mimic the natural swimming performance of fish [5]. These mechanical structures can mainly be categorized into discrete rigid structures [6], [7] and continuous soft structures [8], [9]. The former structures are mostly composed of motor-driven rigid joints. Over the last decades, such design has developed greatly due to its ease of design, control, and modeling. However, robots with discrete rigid structures may generate high noise outputs and harm marine organisms [10]. Therefore, high-performance underwater swimming robots with quiet, safe propulsion methods are urgently needed.

Benefiting from the rapid development of materials science and intelligent manufacturing, underwater robots with continuous soft structures are becoming popular research subjects [11]. Various smart materials and actuators have been developed for soft robotic fish, including shape memory alloys [12], [13], dielectric elastomers [14], [15], ionic polymer–metal composites [16], hydrogels, liquid metals [17], wire-driven actuators [18], [19] and hydraulic/pneumatic actuators [20]. Compared with traditional rigid robots, soft robots have higher degrees of freedom (DOFs) and can absorb large amounts of collision energy. In addition, they have low noise and environmentally friendly characteristics, which have further expanded their applications.

As a mature actuation approach, pressure actuators with large deformation and actuating loads are closer to practical applications than smart materials. In recent years, researchers have successfully applied pressure actuation (e.g., pneumatic, hydraulic, and chemical reaction actuation) to soft underwater robots. In 2014, Marchese et al. described an autonomous untethered soft-bodied robot that can perform rapid continuous-body motion [8]. The robot uses a pneumatic actuator to emulate fish-like escape responses. Compared with pneumatic actuators, hydraulic actuators have a higher response speed and loading capacity due to the incompressibility of the liquid

This article has been accepted for publication in IEEE Transactions on Robotics. This is the author's version which has not been fully edited and content may change prior to final publication. Citation information: DOI 10.1109/TRO.2025.3526087

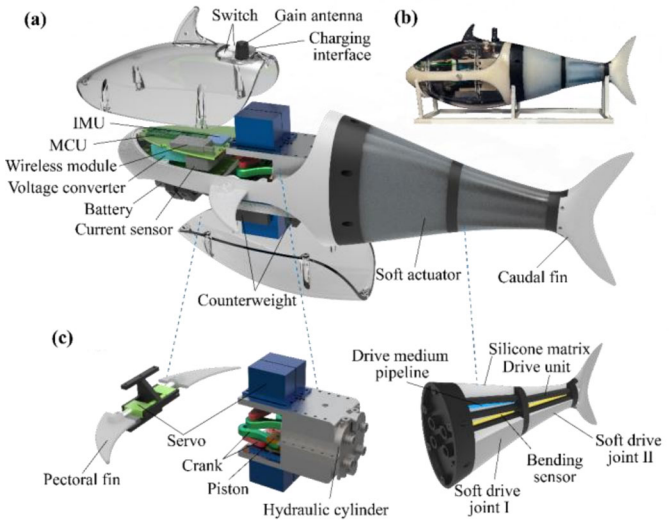

Fig. 1. Overview of HyperTuna design. (a) Overall scheme design. (b) Physical prototype. (c) Scheme design of key components.

medium. SoFi is a widely known hydraulically driven robotic fish [21] developed by Katzschmann et al. Sofi adjusts the undulation behavior of its tail hydraulic actuator to swim forward or turn. The actuating pressure is generated by a displacement pump inside its body. However, pressure-actuated soft underwater robots also have disadvantages. For example, lightweight, miniaturized control valves and pressure pumps are difficult to fabricate. The low drive frequency of such robots also limits their performance.

Achieving accurate perception and control is a challenge for all soft underwater robots. Position feedback can help underwater robots perceive the deformation of their pressure actuators and form effective closed-loop control strategies. In 2018, Engeberg and his team developed a free-swimming soft robotic jellyfish [22]. They established a proportional–derivative controller based on flexible sensors embedded in the tentacles and successfully controlled the angular posture of the tentacles. However, due to the lack of appropriate sensing methods, current body and/or caudal fin soft robots mainly rely on simple open-loop control. Accurate control and intelligent decision-making are difficult to achieve on such robot platforms.

In response to the above problems, in this study, we present HyperTuna, a hydraulically powered double-joint soft robotic fish. In a previous work, we developed a single-joint soft robotic fish and explored how the stiffness of the caudal handle affected its swimming performance [23]. Compared with this previous robot, HyperTuna has more drive joints and piston pump cylinders but has lower volume and weight. These features improve its integration and energy output. Moreover, with embedded bending sensors, a closed-loop controller was built, enabling HyperTuna to control the bending angle of the soft actuator during swimming. We also established a Lagrangian dynamic model for HyperTuna based on multibody dynamics. A data-driven identification method was implemented to estimate the hydrodynamic parameters in the dynamic model. Benefiting from experimental data reflecting different conditions, the effectiveness of the obtained model was also validated. Then, based on the established dynamic model, we used a particle swarm optimization (PSO) algorithm to optimize the action control parameters of HyperTuna to achieve the best swimming state. Finally, we conducted 3-D swimming and long-distance experiments in open water to verify the endurance and practical application potential of HyperTuna.

II. METHODS

A. Mechanical Design of Robotic Fish

In nature, tunas are known for their fast swimming and long-distance cruising capability [24]. Their most significant external features are their spindle-shaped bodies and high-aspect-ratio caudal fins. Based on the appearance of tunas, we develop a hydraulically powered double-joint soft robotic fish called HyperTuna. Its structure is mainly composed of a rigid head and a soft tail, as illustrated in Fig. 1(a). The head integrates control, power, and drive systems. The control system includes a microcontroller unit (MCU) and a communication module. It also has an inertial measurement unit (IMU) and two current sensors, which are used to monitor its own and external environmental information. The power system includes a lithium-ion battery and two voltage converters; these converters provide stable voltages for the control and drive systems. In addition, counterweights are distributed below the buoyancy center to adjust the barycenter and prevent lateral rolling. Fig. 1(b) shows the practical prototype of HyperTuna.

As shown in Fig. 1(c), the drive system includes a pair of pectoral fins for 3-D motion and a four-cylinder piston pump. The pectoral fins and hydraulic pumps (cylinders) are all driven by servos. Changing the pitch angle of the pectoral fins during swimming can help HyperTuna achieve diving–floating movements. The tail actuator has two soft-drive joints with similar structures. In each joint, McKibben artificial muscles as drive units are arranged in pairs on both sides of the body axis. Similar to biological muscles, they expand radially and contract axially under pressure [25]. Joints I and II are composed of five and three drive unit pairs, respectively. A soft bending sensor is located along the body axis in each joint. Joint I is embedded with two additional oil pipelines for joint II in the neutral layer. A silicone matrix envelops the entire joint for shaping, protecting the internal components and transmitting force. The silicone matrix and hoses inside the drive units are made of Ecoflex 00-50 (EC50) and Dragon Skin 10 (DR10), respectively. Table I shows the characteristic parameters of the silicone materials. The manufacturing process of the soft actuator is in Supplementary Information. The main components, including the shells and fins, are 3-D printed. The piston pump is machined from an aluminum alloy. The main specifications of HyperTuna are shown in Table I.

This article has been accepted for publication in IEEE Transactions on Robotics. This is the author's version which has not been fully edited and content may change prior to final publication. Citation information: DOI 10.1109/TRO.2025.3526087

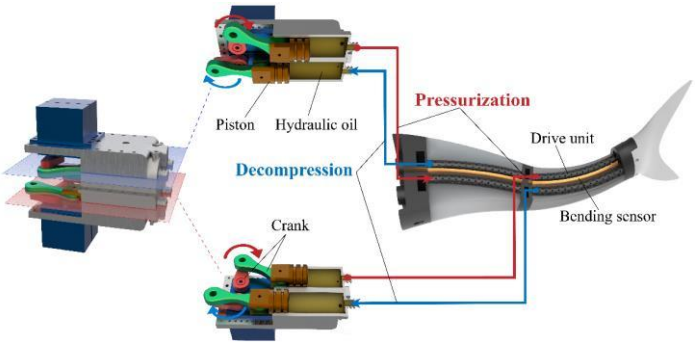

Fig. 2. Mechanism schematic and working principle of HyperTuna.

TABLE I
TECHNICAL SPECIFICATIONS OF HYPERTUNA

Item	Specifications		
Dimensions	520 mm (L) × 206 mm (W) × 172 mm (H)		
Weight	3.3 kg		
MCU	Teensy 4.1 DEV-16771 NXP		
IMU	JY931		
Servos	4.84 kg·cm × 2 (pectoral fins) 70 kg·cm × 4 (piston pump)		
Current sensor	ACS712 5A		
Bending sensor	Flex sensor 4.5		
Pressure sensor	XGZP6858A		
Wireless module	ATK-LORA 433 Mhz		
Battery	Li-ion 18650 3,500 mAh × 4		
Silicone	Tensile strength	100% modulus	Shore hardness
EC50	315 psi	12 psi	00–50
DR10	475 psi	22 psi	10A

B. Working Principle

As shown in Fig. 2, the four hydraulic pumps drive the four groups of drive units of joints I and II. Each hydraulic pump and the corresponding drive unit group form an independent, closed hydraulic system, and the drive medium is hydraulic oil (L-HM46). Each system pressure is monitored using a miniature pressure sensor connected to the hydraulic cylinder. The servos actuate the pistons to control the oil pressure through slider-crank mechanisms. The two piston cylinders work together as a group to drive one joint. The alternating rotation of the servos provides pressure pulses for the joints. As hydraulic oil is pumped into one side of the drive units, the drive units contract under pressure, causing the corresponding joint to bend. Meanwhile, the piston cylinder on the opposite side sucks hydraulic oil out of the connected drive units. This process is circulated during swimming. Therefore, the tail-beat frequency and amplitude and the bending phase difference between the two joints can be controlled by setting the rotational velocity, angle, and cycle of the servos. Compared with using one servo to drive two pistons to move alternately and then control one joint's DOF, using two servos to control the antagonistic drive units independently can improve the drive pressure, avoid generating a negative pressure in the hydraulic system, and expand the drive modes.

C. Deformation Analysis of Actuator

The arrangement density of the drive units is uniform in the matrix, so we cut the actuator axially into slender bodies of equal widths for analysis, with each body containing a set of drive units and a surrounding matrix. Each slender body is considered a cantilever beam. When the unilateral drive units contract and bend the actuator, the central axis surface of the slender body is regarded as a bent neutral layer. In the 2-D schematic diagram in Fig. 3, S is the arc length of the neutral layer and its length remains constant. The mechanical equation of the whole cantilever beam is

$$MS = EI\alpha, \tag{1}$$

where M is the resultant moment acting on the cantilever beam, E is the elastic modulus of the matrix, and I is the moment of inertia of the cross section. In our design, the cross section of the robotic fish is elliptical, so the area moment of inertia $I = \pi ab^3/4$, where a and b are the semimajor and semiminor axes of the cross section, respectively. α is the deflection angle of the actuator. The contraction force direction of the drive units is the axis direction, and it is expressed as

$$bF = \frac{M}{w}, \tag{2}$$

where b is the number of drive units ($b = 5$ in joint I and $b = 3$ in joint II) and w is the distance from the contractility to the neutral layer. In addition, under ideal deformation conditions, α and L have a definite geometric relationship. The lengths of the drive unit L and the neutral layer S have the same center and center angle, and their geometric relationship is expressed as

$$\frac{S}{\alpha} = \frac{L}{\alpha} + w. \tag{3}$$

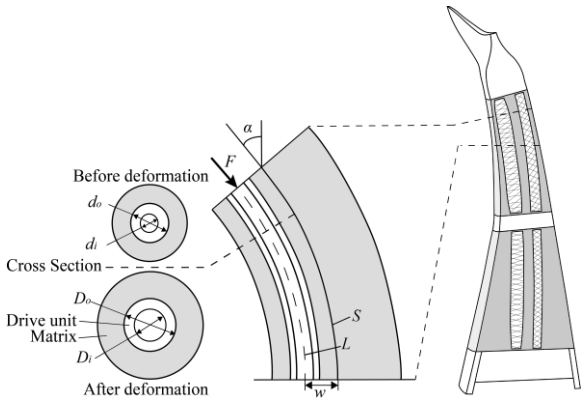

Fig. 3. Simplified actuator bending diagram. Left: schematic diagram before and after deformation of same cross section. Right: axial section of actuator.

This article has been accepted for publication in IEEE Transactions on Robotics. This is the author's version which has not been fully edited and content may change prior to final publication. Citation information: DOI 10.1109/TRO.2025.3526087

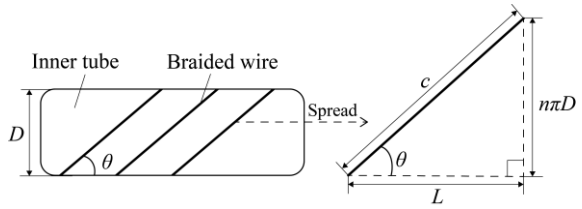

Fig. 4. Geometry of braided nets. Left: helically wound wire forming part of the braided nets. Right: unwound wire showing how the dimensions are related geometrically.

We extend the McKibben shrinkage model established by Ball et al. [26] to analyze the deformation process of the soft actuator. F has four components.

$$F = F_b - F_p + F_t - C_f P_b, \tag{4}$$

where F_b is the axial binding force created by braided nets, F_p is the axial pressure generated by intraluminal fluid, and F_t is the axial elastic force of McKibben's inner tube. $C_f P_b$ is the friction between the braided nets and silicone, which has a hysteresis effect on actuator bending. Here, the friction between the intersection of the braided strands is ignored. C_f is the coefficient of friction and p_b is the positive pressure between the braided nets and the inner tube. The helical wires of the braided nets determine the relationship between the volume and length of the drive units, as shown in Fig. 4. Each wire has a fixed length c and an angle of θ from the axial direction; n is the number of turns wrapped around the inner hose. Thus, the length of the drive unit $L = c \times cos\theta$. The outer diameter of the inner hose is $D = c \times sin\theta/(n\pi)$, $D^2 = c^2 sin^2\theta/n^2\pi^2 = c^2(1 - cos^2\theta)/n^2\pi^2$, and $cos^2\theta = L^2/b^2$. Excluding the thickness of the braided nets, the volume of the wrapped braided nets is

$$V = \frac{\pi D^2}{4} L = \frac{c^2 L - L^3}{4\pi n^2}. \tag{5}$$

V_t is the volume of the inner tube, and it is constant because the silicone tube is incompressible. Then, the volume V_f of the inner fluid after deformation is

$$V_f = V - V_t = \frac{c^2 L - L^3}{4\pi n^2} - \frac{\pi}{4}(d_o^2 - d_i^2)L_0, \tag{6}$$

where L_0 is the initial length of the drive units and $L_0 = S$. d_o and d_i are the outer and inner diameters, respectively, of the inner tube before deformation. The inner diameter of the inner tube after deformation is $D_i = 2\sqrt{V_f/\pi L}$. The Mooney–Rivlin model of incompressible solids is used to analyze the silicone elastomer. The strain energy density function W is

$$W = C_1(\lambda_1^2 + \lambda_2^2 + \lambda_3^2 - 3) + C_2(\lambda_1^2\lambda_2^2 + \lambda_2^2\lambda_3^2 + \lambda_3^2\lambda_1^2 - 3), \tag{7}$$

where C_1 and C_2 are coefficients related to the materials. λ_1, λ_2, and λ_3 are the principal stretch ratios along the cylinder axis, circumference, and radius, respectively. The true stress relationships are

$$\sigma_{11} - \sigma_{33} = 2C_1(\lambda_1^2 - \lambda_3^2) - 2C_2\left(\frac{1}{\lambda_1^2} - \frac{1}{\lambda_3^2}\right), \tag{8}$$

$$\sigma_{22} - \sigma_{33} = 2C_1(\lambda_2^2 - \lambda_3^2) - 2C_2\left(\frac{1}{\lambda_2^2} - \frac{1}{\lambda_3^2}\right). \tag{9}$$

For the inner tube, $\lambda_{t1} = L/L_0$; $\lambda_{t2} = D_i/d_i$; $\lambda_{t3} = 1/\lambda_{t1}\lambda_{t2}$; and the circumferential and axial engineering stresses are

$$\sigma_{t11} = \sigma_{t33} + \lambda_{t2}\lambda_{t3}\left(2C_1(\lambda_{t1}^2 - \lambda_{t3}^2) - 2C_2\left(\frac{1}{\lambda_{t1}^2} - \frac{1}{\lambda_{t3}^2}\right)\right), \tag{10}$$

$$\sigma_{t22} = \sigma_{t33} + \lambda_{t1}\lambda_{t3}\left(2C_1(\lambda_{t2}^2 - \lambda_{t3}^2) - 2C_2\left(\frac{1}{\lambda_{t2}^2} - \frac{1}{\lambda_{t3}^2}\right)\right), \tag{11}$$

where σ_{t33} is approximately the internal fluid pressure $-P$. The circumferential force in a segment $\mathrm{d}L$ of the inner tube is

$$\mathrm{d}F_{tc} = (P - P_t) \times \frac{D_i \mathrm{d}L}{2} = \frac{\sigma_{t22}(d_o - d_i)\mathrm{d}L}{2}, \tag{12}$$

where P_t is the pressure on the outside of the inner tube and

$$P_t = P - \frac{\sigma_{t22}(d_o - d_i)}{D_i}. \tag{13}$$

The outer side of the inner tube is subjected to the circumferential force P_b of the braided nets and the circumferential force P_s of the external matrix, and $P_t = P_b + P_s$. The external matrix is equivalent to a tube and is calculated according to the Mooney–Rivlin model with zero outermost pressure. Given m strands that are each wound around the inner tube n times, the strands cross the cut in $2mn$ places such that the circumferential component of force along each is

$$F_c = \frac{P_b D_o L}{2mn} = \frac{(P_t - P_s)D_o L}{2mn} = F_w \sin\theta, \tag{14}$$

where F_w is the force on each strand. The axial force generated by the braided nets is

$$F_b = mF_w \cos\theta = \frac{mF_c}{tan\theta}, \tag{15}$$

and

$$F_p = P\frac{V_f}{L}, \tag{16}$$

$$F_t = \frac{\sigma_{t11} V_t}{L}. \tag{17}$$

Therefore, the relationship between the air pressure P and the deflection angle α of the actuator can be obtained by combining Eqs. (2), (3), (4), and (18). Let the actuator be divided into k parts, with the deflection angle of each part denoted as α_i $(i = 1, 2, \ldots, k)$; then, the total bending angle of the actuator is

$$\beta = \sum_{i=1}^{k} \alpha_i. \tag{18}$$

D. Establishment of Swimming Dynamic Model

A 2-D dynamic model for HyperTuna combining Lagrangian modeling and multibody dynamics is established in this section to provide a basis for the optimization of control parameters.

1. Coordinate Frames and Notations

Swimming dynamic modeling has two main types: multibody dynamics and beams [27] [28] [29]. Multibody dynamic models are more widely used due to their greater accuracy, although they have limitations, such as high complexity and a large number of parameters. Here, a classic pseudorigid-body

This article has been accepted for publication in IEEE Transactions on Robotics. This is the author's version which has not been fully edited and content may change prior to final publication. Citation information: DOI 10.1109/TRO.2025.3526087

(PRB) 3R (where R represents a revolute joint) model is used

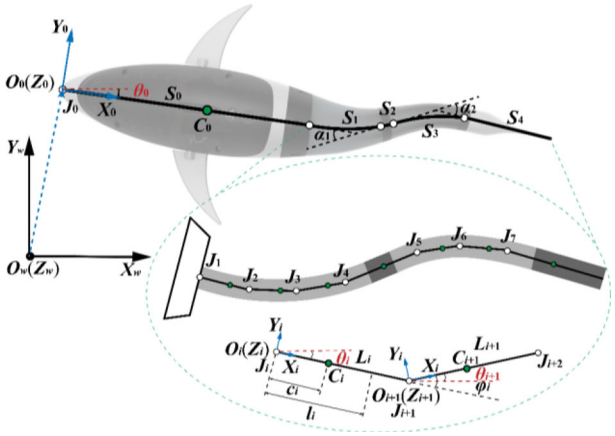

Fig. 5. Schematic diagram of coordinate systems and notations.

to approximate soft-joint deflection [30] [31]. The PRB 3R model has good simulation accuracy despite using limited computing resources. In Fig. 5, S_0 represents the head. We use a multipseudolink model to approximate the soft joints S_1 and S_3, connector S_2, and caudal fin S_4 as seven virtual rigid links L_i, $i \in [1,7]$. Therefore, joints I and II are simplified as rigid joints $J_{2\text{-}4}$ and $J_{5\text{-}7}$, respectively.

As illustrated in Fig. 5, $\{O_w - X_wY_wZ_w\}$ is the world coordinate system. The attached coordinate systems $\{O_i - X_iY_iZ_i\}$, $i \in [0,7]$, are attached to L_i. The origin O_i is fixed on joint J_i, and the axis X_i is parallel to L_i. Planes $\{O_wX_wY_w\}$ and $\{O_iX_iY_i\}$ are fixed on the water surface. All coordinate systems follow the right-hand rule. The mass and length of L_i are m_i and l_i, respectively. The center of mass (CM) of L_i is C_i, and the distance between J_i and C_i is c_i. φ_i is the absolute rotation angle of J_i. θ_i is the angle between the axis X_w and L_i. α_1 and α_2 represent the bending angles of the two soft-drive joints and are actively controlled through closed-loop control. All angles defined in this research follow the right-hand rule. According to the kinematic relation, angles φ_i and θ_i are expressed as

$$\varphi_2 = \varphi_3 = \varphi_4 = \frac{\alpha_1}{3}, \tag{19}$$

$$\varphi_5 = \varphi_6 = \varphi_7 = \frac{\alpha_2}{3}, \tag{20}$$

$$\theta_i = \theta_{i-1} + \varphi_i, (i \in [1,7]). \tag{21}$$

The rotating transformation matrix ${}^wR_i$ of $\{O_i - X_iY_iZ_i\}$ with respect to $\{O_w - X_wY_wZ_w\}$ and the position vector ${}^{i-1}P_i$ of O_i with respect to C_{i-1} are

$${}^wR_i = \begin{bmatrix} cos\theta_i & -sin\theta_i & 0 \\ sin\theta_i & cos\theta_i & 0 \\ 0 & 0 & 1 \end{bmatrix}, {}^{i-1}P_i = \begin{bmatrix} l_{i-1} \\ 0 \\ 0 \end{bmatrix}. \tag{22}$$

The position vector ${}^wr_i$ of C_i in the world coordinate system is expressed as

$${}^wr_i = {}^wR_i\,{}^ir_i + {}^wP_i, \tag{23}$$

$${}^wP_i = {}^wP_0 + \sum_{j=1}^{i} {}^wR_{j-1}\,{}^{j-1}P_j, \tag{24}$$

where ${}^ir_i$ is the position vector of C_i in the coordinate system $\{O_i - X_iY_iZ_i\}$, ${}^wP_i$ is the position vector of O_i in the coordinate system $\{O_i - X_iY_iZ_i\}$, and ${}^wP_0 = [X_0, Y_0, 0]^T$ is the position vector of O_i in $\{O_w - X_wY_wZ_w\}$. The translational velocity ${}^wv_i = [{}^wv_{x,i}\ {}^wv_{y,i}, {}^wv_{z,i}]^T$ of C_i with respect to $\{O_w - X_wY_wZ_w\}$ is expressed as

$${}^wv_i = {}^w\dot{r}_i = {}^w\dot{R}_i{}^wr + {}^wR_i{}^w\dot{r}_i + {}^w\dot{P}_i, \tag{25}$$

where ${}^w\dot{R}_i = S({}^ww_i){}^wR_i$, $S({}^ww_i)$ is a skew-symmetric matrix of ${}^ww_i$. The angular velocity of C_i in the world coordinate system is

$${}^ww_0 = [0\ \ 0\ \ \dot{\theta}_0]^T, \tag{26}$$

$${}^ww_i = {}^ww_{i-1} + {}^wR_i\,{}^iw_i, (i \in [1,7]), \tag{27}$$

where ${}^ww_i = [{}^ww_{x,i}\ {}^ww_{y,i}, {}^ww_{z,i}]^T$, ${}^iw_i = [0\ \ 0\ \ \dot{\varphi}_i]^T$.

2. Lagrangian Dynamic Modeling

We use Euler–Lagrange equation to establish the dynamic model of HyperTuna. The model has three DOFs. They are positions x_0 and y_0 and the rotation angle θ_0 of the coordinate system $\{O_i - X_iY_iZ_i\}$ relative to the world coordinate system. The generalized coordinate q and velocity $\dot{q}$ are expressed as

$$q = [x_0, y_0, \theta_0]^T, \tag{28}$$

$$\dot{q} = [\dot{x}_0, \dot{y}_0, \dot{\theta}_0]^T. \tag{29}$$

The Lagrange multiplier $\mathcal{L}(q,\dot{q},t)$ is the difference between the kinetic energy $T(q,\dot{q},t)$ and potential energy $E(q,\dot{q},t)$ of the system, and it is expressed as

$$\mathcal{L}(q,\dot{q},t) = T(q,\dot{q},t) - E(q,\dot{q},t), \tag{30}$$

where $T(q,\dot{q},t)$ is

$$T(q,\dot{q},t) = \sum_{i=0}^{7} \frac{1}{2}{}^wv_i{}^TM_i{}^wv_i + \sum_{i=0}^{7} \frac{1}{2}{}^ww_i{}^TI_i{}^ww_i, \tag{31}$$

where M_i and I_i are the mass matrix and inertia tensor, respectively. HyperTuna does not pitch during straight swimming; its gravitational potential energy remains constant. Therefore, the system has no potential energy, i.e., $E(q,\dot{q},t) = 0$. Lastly, the Lagrangian dynamic model is

$$\frac{d}{dt}\frac{\partial \mathcal{L}}{\partial \dot{q}} - \frac{\partial \mathcal{L}}{\partial q} = [F_x\ F_y\ T_0\ ]^T, \tag{32}$$

where the generalized forces F_x and F_y are the components of the hydrodynamic forces on axes X_w and Y_w, respectively. The generalized moment T_0 is the moment generated by the hydrodynamic forces acting on the virtual joint J_0.

3. Hydrodynamic Force Analysis

The hydrodynamic forces acting on HyperTuna include added mass force and drag force. The number of unknown parameters in the model is minimized by defining the added mass force ${}^wF_{a,i}$ of the link L_i in world coordinate system as

$${}^wF_{a,i} = [{}^wF_{ax,i}\ {}^wF_{ay,i}\ {}^wF_{az,i}]^T = -c_{m,i}m_i[{}^w\dot{v}_{x,i}\ {}^w\dot{v}_{y,i}\ 0]^T, \tag{33}$$

where ${}^wF_{ax,i}$, ${}^wF_{ay,i}$, and ${}^wF_{az,i}$ are the added mass forces along the three coordinate axes of the world coordinate system,

and they act on the CM C_i. $c_{m,i}$ is the uniform added mass coefficient in all directions, and m_i is the mass of C_i. The drag force of C_i is expressed as

$$^{w}F_{d,i} = {}^{w}R_i\,{}^{i}F_{d,i}, \tag{34}$$

$$^{i}F_{a,i} = \begin{bmatrix} {}^{i}F_{dx,i} \\ {}^{i}F_{dy,i} \\ {}^{i}F_{dz,i} \end{bmatrix} = \begin{bmatrix} -\frac{1}{2}c_{f,i}\rho S_{x,i}\left|{}^{i}v_{x,i}\right|{}^{i}v_{x,i} \\ -\frac{1}{2}c_{d,i}\rho S_{y,i}\left|{}^{i}v_{y,i}\right|{}^{i}v_{y,i} \\ 0 \end{bmatrix}, \tag{35}$$

where $^{w}F_{d,i}$ and $^{i}F_{d,i}$ are the drag forces of C_i in $\{O_w - X_wY_wZ_w\}$ and $\{O_i - X_iY_iZ_i\}$, respectively. $^{i}F_{dx,i}$, $^{i}F_{dy,i}$, and $^{i}F_{dz,i}$ are the added mass forces along the three coordinate axes of the coordinate system $\{O_i - X_iY_iZ_i\}$. $c_{f,i}$ and $c_{d,i}$ are the friction and drag coefficients, respectively, of the virtual link L_i. ρ is the fluid density. $^{i}v_{x,i}$ and $^{i}v_{y,i}$ are the translational velocities of C_i in $\{O_i - X_iY_iZ_i\}$. Finally, the generalized forces and moment are

$$\begin{cases} F_x = \sum_{i=0}^{7} {}^{w}F_{ax,i} + \sum_{i=0}^{7} {}^{w}F_{dx,i} \\ F_y = \sum_{i=0}^{7} {}^{w}F_{ay,i} + \sum_{i=0}^{7} {}^{w}F_{dy,i} \\ T_0 = \sum_{i=0}^{7} {}^{w}T_{a0,i} + \sum_{i=0}^{7} {}^{w}T_{d0,i} \end{cases}, \tag{36}$$

where $^{w}T_{a0,i}$ and $^{w}T_{d0,i}$ are the moments acting on the virtual joint J_0 caused by the added mass force and drag force, respectively.

III. RESULTS

A. Actuator Bending Test in Air

In the bending test, the pressure of the actuator was adjusted using the hydraulic pump based on feedback signals from the pressure sensor of the system. Similar testing methods were used under the four operating conditions in Fig. 6(a). For example, as joint I bent right, the drive unit groups were inactive except that on the right side of joint I, which was pressurized. The actuator bending tests were performed at 100–250 kPa. The bending angles were converted from the analog outputs of the bending sensors. As shown in Fig. 6(e), the bending angles of the two joints show a linear trend with the drive pressure. The maximum bending angle of joint II is larger than that of joint I because it contains less silicone matrix. Meanwhile, the deflection angles of the same joint in the two directions slightly differ, possibly due to manufacturing accuracy. The ultimate bending angles of joints I and II are 18.2° and 31.2°, respectively, satisfying the required beat amplitude for robotic fish [6] [32] [33]. The calculated bending angles based on the theoretical deformation analysis of the actuator above are plotted in Fig. 6(e). Despite the errors between the calculated and experimental results, their trends are consistent, indicating that the theoretical analysis model of the actuator has certain reference value.

B. Simulation Analysis of Actuator Deformation

An FE method (FEM) based on ABAQUS (Dassault Systèmes) was built to investigate the deformation response of the soft actuator. To simulate the actuator response, we modeled the drive units as closed circular tubes driven by a fluid cavity. Double-symmetrical-layer rebars were set on the closed circular tubes to simulate the woven braided nets on the drive units, whose Young's modulus and Poisson's ratio were 100 MPa and 0.3, respectively. Under the pressure of the inner cavity, the closed circular tube in the simulation generated radial expansion and axial contraction like a drive unit, as shown in Fig. 6(d). The circular tube and matrix of the actuator were defined as linear elastic materials, with Young's modulus and Poisson's ratios of 0.15 MPa and 0.3 for the former and 0.08 MPa and 0.475 for the latter. The interaction between the drive units and the matrix was set as a tie constraint. The connector at the end of the actuator was completely fixed, whereas the tail fin was free. The drive units of joints I and II were meshed with 1,364 and 834 quadrilateral linear (S4R) elements, respectively. The matrices of joints I and II were meshed with 37,648 and 10,965 tetrahedral linear (C3D4) elements, respectively. The connectors and caudal fin were defined as rigid bodies. The actuator strain and stress at the same drive pressure in the bending test are shown in Figs. 6(b) and 6(c), respectively. A comparison between the simulation and the test (Fig. 6(a)) shows similar deformation at each pressure. All FEM simulations reveal similar deformation, all increasing with the load, which is consistent with the experimental results. The actuator strain and stress are mainly concentrated on the drive units and the surrounding flexible matrix. The experimental and simulated bending angles per actuator are compared in Fig.6(e).The

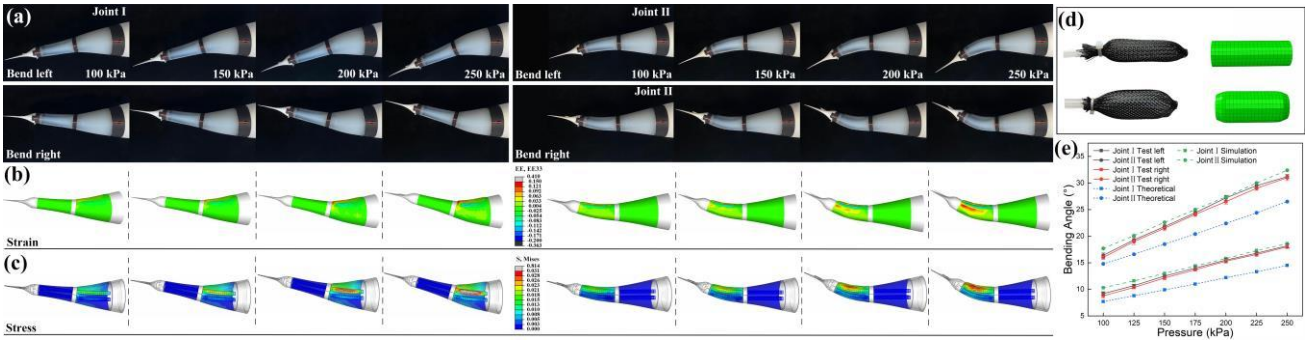

Fig. 6. Actuator bending test and finite element (FE) simulation. (a) Snapshots of bending test at different drive pressures. (b)(c) Actuator strain and stress at different drive pressures based on FE model. (d) Comparison of drive unit and its FE model before

and after contraction. (e) Bending angles at different pressures. The error bars represent the standard deviation of the mean (n = 5).

FEM simulations accurately predict the bending angle (negligible error) and consistently match the experimental data at different drive pressures.

C. Closed-Loop Control

HyperTuna is controlled using a model that combines a proportional–integral–derivative (PID) controller with a central pattern generator (CPG), as shown in Fig. 7. The CPG controller is built based on Hopf oscillators, whose output signals converge to sine waves. Each servo of HyperTuna is controlled by a separate oscillator. The coupling relationships between adjacent oscillators form the CPG network. We use the phase of CPG1 as a reference and transfer the phase constraints of the remaining oscillators through the coupling relationships. The linear system of ordinary differential equations for the ith oscillator is expressed as

$$\begin{cases} \dot{x}_i = -\omega y_i + k x_i (x_i - b_i)(A_i^2 - (x_i - b_i)^2 - y_i^2) + \\ \qquad h_{j,i}\left((x_j - b_j)cos\Phi_{j,i} + y_i sin\Phi_{j,i}\right) \\ \dot{y}_i = -\omega(x_i - b_i) + k y_i (A_i^2 - (x_i - b_i)^2 - y_i^2) \end{cases}, \quad (37)$$

where x_i and y_i represent the state variables of the excitatory and inhibitory neurons, respectively, of the ith oscillator. In this study, x_i is the output signal used to control the servos. ω, A_i, and b_i are the frequency, amplitude, and bias of the ith oscillator, respectively. k denotes the convergence factor. $h_{j,i}$ and $\Phi_{j,i}$ are the coupling weight and phase difference, respectively, between the ith and jth oscillators. For the tail fin oscillator, the bias $b_i = A_i$. For the pectoral fin oscillator, the amplitude $A_i = 0$, and the angle of attack of the pectoral fins is changed by adjusting the bias b_i. Φ_{13} represents the phase difference between the two joints.

In practical operations, accurately controlling the joint bending angle in each swing cycle through closed-loop control is difficult. Therefore, here, the PID controller intervenes to adjust the amplitude of the CPG controller at the end of each swing cycle. Specifically, at the end of the swing cycle, the PID controller automatically calculates the maximum servo angle according to the error between the set and actual maximum joint bending angles and transmits it to the CPG controller as the amplitude for the next cycle, as shown in Fig. 7.

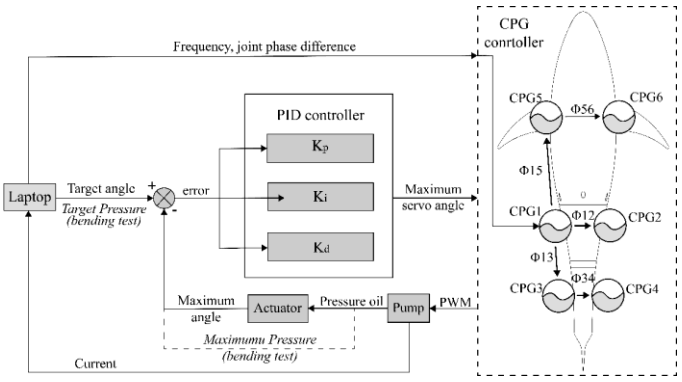

Fig. 7. Schematic diagram of PID–CPG closed-loop control.

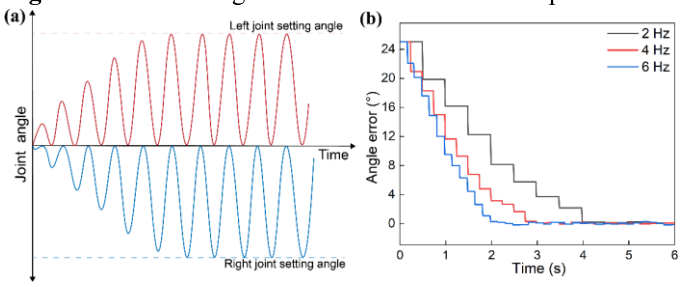

Fig. 8. Closed-loop control effect of joint angle. (a) Joint angle adjustment process. (b) Joint angle error (set angle: 20°).

The features of the CPG allow it to generate smooth control signals despite the alterations in amplitude. The CPG controller outputs are converted into pulse-width modulation signals and transmitted to the servos to generate motion. The whole control cycle runs at 100 Hz. Finally, the joint angle gradually increases and reaches the set value after a few swing cycles. A schematic diagram of the adjustment process of the joint angle is shown in Fig. 8(a). The actual joint angle error is shown in Fig. 8(b). The joint angle can converge to 0 within 4 s at all drive frequencies, and the higher the frequency, the faster the convergence.

D. Swimming Test in Water

We conducted a free-swimming test in a water tank sized 4 m × 2 m × 1 m. The robot maintained straight motion in the swimming test, the pectoral fin servos remained stationary, and the pectoral fins were kept horizontal. The speed of HyperTuna was obtained by integrating the acceleration measured by the IMU. We recorded the average swimming speed over the last half interval as the measured speed for a single swimming test. The critical variables affecting HyperTuna's performance include the beat frequency, amplitude, and the phase difference between the two joints. Therefore, we focused on the influence of these parameters in the CPG on swimming performance before developing an efficient control strategy for HyperTuna. Based on the actuator bending test in air, we divided the beat amplitude into three levels: small amplitude (the bending angles of joints I and II are 8° and 15°, respectively), medium amplitude (12° and 20°, respectively), and large amplitude (16° and 25°, respectively). The experiments were conducted at different beat amplitude levels, frequencies, and phase differences. In the swimming test, the pressure sensor monitored the system pressure in real time to ensure that the system pressure did not exceed the upper limit and damage the flexible actuator in case the bending sensor failed. Fig. 9 shows snapshots of the swimming test at a drive frequency of 3 Hz, a joint phase difference of 20°, and a me-

This article has been accepted for publication in IEEE Transactions on Robotics. This is the author's version which has not been fully edited and content may change prior to final publication. Citation information: DOI 10.1109/TRO.2025.3526087

dium beat amplitude.

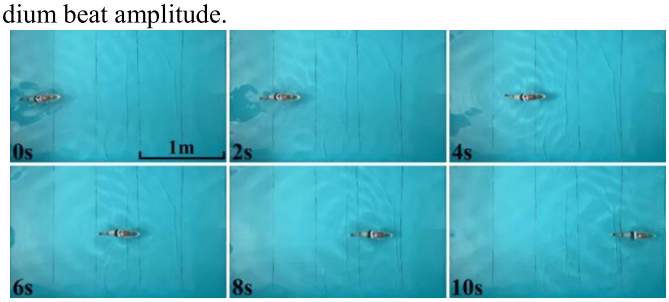

Fig. 9. Snapshots of swimming test at 3 Hz, 20° phase difference, and medium beat amplitude.

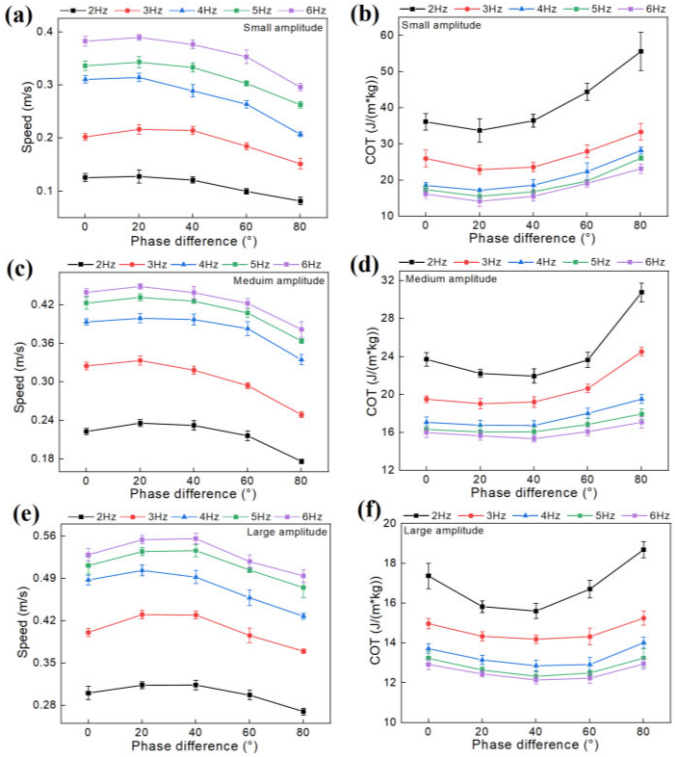

Fig. 10. Swimming performance of HyperTuna under different operating conditions. (a) (b) Speed and COT at small beat amplitude. (c) (d) Speed and COT at medium beat amplitude. (e) (f) Speed and COT at large beat amplitude. The error bars represent the standard deviation of the mean (n = 5).

Directly obtaining the efficiency of underwater robots is difficult. In this study, we introduced the cost of transport (COT) to reflect the motion efficiency of HyperTuna. COT is the energy consumption per unit distance.

$$COT = \frac{Q}{l} = \frac{P}{U} = \frac{\frac{1}{T}\int_0^T EI \ dt}{U}, \tag{38}$$

where l is the unit swimming distance; Q is the energy consumption of the unit swimming distance; P is the input power of the servos; U is the steady forward speed; T is the swing period of the robotic fish; E is the rated voltage of the servos; and I is the instantaneous current flowing through the servos, which is monitored by the current sensor. We only included the servo power in the COT calculation, ignoring the small power of the electronic system. Fig. 10 illustrates the swimming speed of HyperTuna under different operating conditions. A higher beat frequency and amplitude leads to higher speeds but smaller COT values. However, this trend—increasing speed and decreasing COT—slows down as the frequency increases. This is consistent with other types of robotic fish [34], [35], [36]. Note that the effect of the joint phase differences on swimming performance is not monotonic. This result is similar to those in prior multijoint robotic fish studies [24], [37]. Moreover, the optimal joint phase differences for swimming speed and COT are almost the same under most conditions, with a larger beat amplitude leading to a larger optimal phase difference. For example, the optimal phase difference is 20° at the small beat amplitude but 40° at the large beat amplitude. Therefore, adjusting the phase difference is one way to optimize swimming performance. Finally, HyperTuna reaches its maximum speed of 1.08 BL/s (0.56 m/s) at 6 Hz, a 40° phase difference, and the large beat amplitude; it is faster than previously reported hydraulic robotic fish [21], [38], [39]. At the same control parameters, HyperTuna also has the lowest COT of 12.15 J/(kg·m), which means that the robotic fish theoretically has a maximum range of 21.12 km with a 14,000 mAh battery.

E. Simulation and Parameter Identification

To further validate the generalization ability of the dynamic model, we established a simulation platform for robotic fish based on the Simscape Multibody module in MATLAB (MathWorks). Furthermore, a PSO algorithm was used to optimize the control parameters for HyperTuna online based on the simulation platform. A simulation block diagram of the system is shown in Fig. 11(a). The CPG controller transmits the motion parameters to the kinematic module. The spatial positions and constraint relations of each virtual link in the kinematic module are consistent with those in the kinematic model in Fig. 5. The kinematic module transmits the speed and acceleration of the virtual links to the mechanics module. Based on the above hydrodynamic force analysis, the mechanics module calculates the force of each link and advances the simulation model. Fig. 11(b) shows snapshots of the swimming simulation at 3 Hz, 20° phase difference, and medium beat amplitude. The PSO optimizer continuously calls simulation models to find the optimal control parameters.

The simulation physical parameters presented in Table II were measured directly. The hydrodynamic parameters were difficult to measure experimentally due to the complex interaction between the robotic fish and the fluid. Therefore, we used Parameter Estimator in Simulink to estimate them. The hydrodynamic parameters included the added mass coefficient

This article has been accepted for publication in IEEE Transactions on Robotics. This is the author's version which has not been fully edited and content may change prior to final publication. Citation information: DOI 10.1109/TRO.2025.3526087

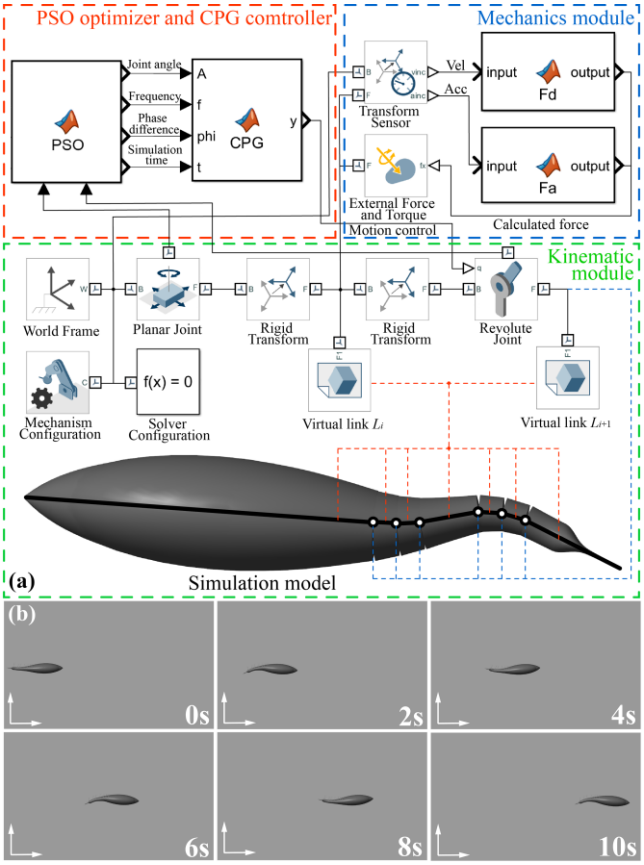

Fig. 11. Simulation and parameter optimization platform. (a) Simulation and parameter optimization process based on Simscape Multibody. (b) Snapshots of swimming simulation at 3 Hz, 20° phase difference, and medium beat amplitude.

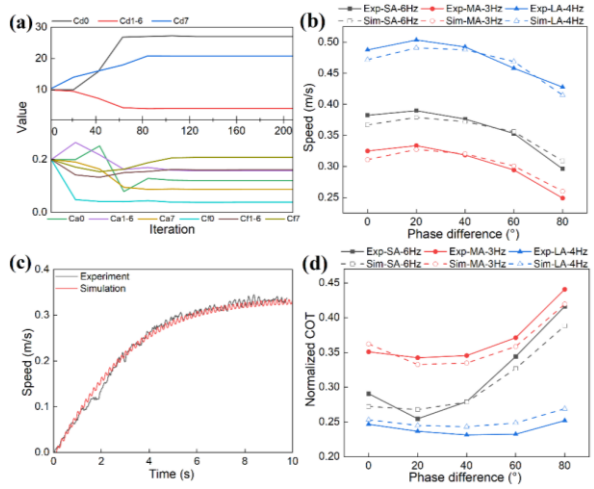

Fig. 12. Parameter identification and verification. (a) Hydrodynamic parameter estimation. (b) Speed comparisons between simulation and validation sets. (c) Instantaneous speed comparison between simulation and experiment for a single swimming process at 3 Hz, 20° phase difference, and medium beat amplitude. (d) Normalized COT comparison of simulation and validation sets. SA stands for small amplitude; MA, medium amplitude; LA, large amplitude.

$c_{m,i}$, friction coefficient $c_{f,i}$, and drag coefficient $c_{d,i}$ of virtual link L_i. For simplicity, the hydrodynamic parameters for $L_{1\text{-}6}$ were assumed to be equal due to their similar appearances.

Finally, there are still nine hydrodynamic parameters to be identified in this study. 80% of the experimental data were randomly selected as the training set, and the rest were selected as the validation set. The optimization boundaries $[\mu_{min}, \mu_{max}]$ and initial values μ_0 of the hydrodynamic parameters are given after a few simulation trials, as tabulated in Table III. As shown in Fig. 12(a), the hydrodynamic parameters converged after 210 rounds of Parameter Estimator iteration. The final identified results μ are listed in Table III.

The simulation and experiment were compared to verify the proposed dynamic model and estimated model parameters. According to Fig. 12(b), the simulation speed agrees with the validation set, with the maximum relative error not exceeding 5%. Specifically, Fig. 12(c) shows the instantaneous speed curves obtained from the simulation and experiment. In the acceleration phase and the steady swimming phase, the motion states in the simulation match those in the actual experiment. In the simulation, the rotations of the virtual joints $J_{2\text{-}7}$ form the swimming motion, and the total output power is equal to the product of the drive torque and angular velocity of each joint. Therefore, the simulation COT is expressed as

$$COT_{sim} = \frac{\frac{1}{T}\int_0^T (\sum_{i=2}^{7} T_i \dot{\varphi}_i) dt}{U}, \tag{39}$$

where T_i is the drive torque of joint J_i. However, due to the energy loss of motion components in actual operation, such as hydraulic systems and actuators, the COT values of the simulation and experiment are not at the same level. To facilitate comparison, we normalized their COT values. As shown in Fig. 12(d), the normalized COT_{sim} follows the same trend as the verification set; the maximum relative error is less than 7%. Finally, the presented results indicate that the constructed simulation model has good generalization ability.

TABLE II
PHYSICAL PARAMETERS OF HYPERTUNA

Item	mi (kg)	l_i (cm)	c_i (cm)	$S_{x,i}$ (cm^2)	$S_{y,i}$ (cm^2)
L_0	2.209	28.1	16.63	337.5	90.3
L_1	0.117	2.0	0.96	23.1	59.3
L_2	0.091	2.0	0.96	20.8	52.8
L_3	0.069	2.0	0.95	18.4	46.1
L_4	0.106	5.0	2.20	35.6	88.8
L_5	0.026	2.0	0.96	10.7	27.1
L_6	0.020	2.0	0.96	9.2	23.7
L_7	0.049	8.9	3.13	51.1	115.4

This article has been accepted for publication in IEEE Transactions on Robotics. This is the author's version which has not been fully edited and content may change prior to final publication. Citation information: DOI 10.1109/TRO.2025.3526087

TABLE III
HYDRODYNAMIC PARAMETERS FOR IDENTIFICATION

Item	μ_{min}	μ_{max}	μ_0	μ
$c_{m,0}$	0	1	0.2	0.12092
$c_{m,1-6}$	0	1	0.2	0.15816
$c_{m,7}$	0	1	0.2	0.0882
$c_{f,0}$	0	1	0.2	0.03845
$c_{f,1-6}$	0	1	0.2	0.16131
$c_{f,7}$	0	1	0.2	0.20809
$c_{d,0}$	0	30	10	27.0706
$c_{d,1-6}$	0	30	10	3.9829
$c_{d,7}$	0	30	10	20.7766

F. PSO-Based Optimization of Control Parameters

We used a PSO algorithm to optimize the CPG network parameters. The PSO algorithm is an evolutionary algorithm with simple content and a few parameters [40]. It implements iterative optimization in an n-dimensional space. The particle updates its position by tracking the individual extremum p_b and global extremum g_b. The particle updating formula is

$$\begin{cases} v_i(t+1) = w \times v_i(t) + c_1 \times rand \times \left(p_b(t) - x_i(t)\right) \\ \qquad\qquad +c_2 \times rand \times \left(g_b(t) - p_i(t)\right) \\ p_i(t+1) = p_i(t) + v_i(t+1) \end{cases}, \quad (40)$$

where $v_i(t)$ and $p_i(t)$ denote the velocity and position, respectively, of the ith particle at time t; w denotes the inertia weight; c_1 and c_2 are the learning factors; and $rand$ is a random number in [0,1]. The joint angles α_1 and α_2, beat frequency ω, and phase difference Φ_{13} form the position space of the particles and meet the conditions

$$\begin{cases} 0 \le \alpha_1 \le 16 \\ 0 \le \alpha_2 \le 25 \\ 0 < \omega \le 6 \\ 0 \le \Phi_{13} \le 80 \end{cases}. \quad (41)$$

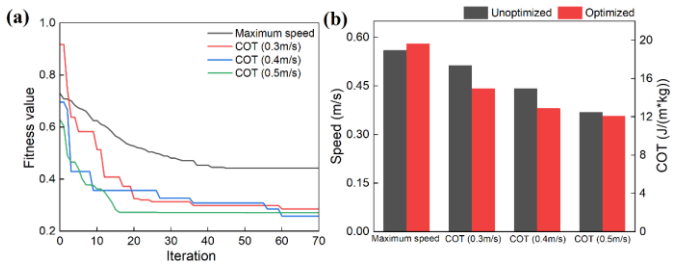

Fig. 13. Parameter optimization using PSO algorithm. (a) Fitness value curve in PSO. (b) Swimming performance before and after optimization.

The fitness function is used to evaluate the particle position to determine whether the position is the optimal solution or a possible optimal solution. Therefore, the optimization objective of the PSO algorithm can be customized through the fitness function. We adopted the fitness function

$$f(x) = |U_{sim} - U_e| + k \times COT_{sim}, \quad (42)$$

where U_{sim} and U_e are the simulation speed and the expected speed, respectively, and k is the adjustment coefficient. The optimization objective is to minimize COT_{sim} while ensuring that the simulation speed U_{sim} is close to the expected speed U_e. Specifically, when the expected speed U_e is greater than the upper speed limit of the robot and the adjustment coefficient $k = 0$, the optimization objective is to find the maximum speed while ignoring COT_{sim}. The lower the particle fitness, the closer it is to the optimization objective. The parameter optimization process is shown in Fig. 11(a). The PSO optimizer calculates fitness values based on the received speed and COT, updates the particle positions, and calls simulation models.

TABLE IV
PARAMETER OPTIMIZATION RESULTS

Expected speed		Maximization	0.3 m/s	0.4 m/s	0.5 m/s
α_1 (°)	Unoptimized	16	16	16	16
	Optimized	15.98	15.62	15.95	15.55
α_2 (°)	Unoptimized	25	25	25	25
	Optimized	4.93	24.31	16.08	20.83
Frequency (Hz)	Unoptimized	6	2	3	5
	Optimized	5.99	2.13	4.75	5.21
Phase difference (°)	Unoptimized	40	0	0	60
	Optimized	37.43	38.56	64.19	51.42

In the PSO algorithm, 15 particles were set to search for the optimal solution. We selected four scenarios to validate the optimization algorithm, including finding the maximum speed and reducing COT_{sim} at U_e = 0.3, 0.4, 0.5 m/s. As shown in Fig. 13(a), the fitness values in each scenario converge after 60 iterations. The parameter optimization results are listed in Table IV. For further verification, the optimal control strategies are applied to HyperTuna. The results before and after optimization are illustrated in Fig. 13(b). The unoptimized data set comes from the above experiments. After optimization, the maximum speed increases by 3.6%, and COT decreases by 13.8%, 13.9%, and 3.2% at the three expected speeds. The experimental results prove that the PSO algorithm can effectively improve the performance of the robotic fish.

G. Verification of Other Basic Functions

Turning and diving–floating are indispensable functions for 3-D swimming. HyperTuna can achieve these functions by controlling the movements of the tail fin and pectoral fins. HyperTuna was tested for turning, diving–floating, and long-distance swimming.

This article has been accepted for publication in IEEE Transactions on Robotics. This is the author's version which has not been fully edited and content may change prior to final publication. Citation information: DOI 10.1109/TRO.2025.3526087

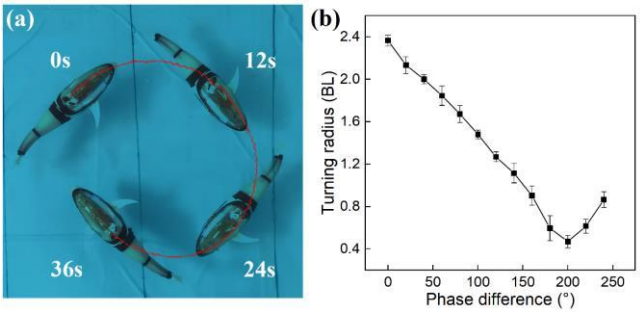

Fig. 14. Turning test. (a) Snapshots of turning process. (b) Turning radius.

1. Turning Test

Robotic fish commonly use the asymmetric swing of their tail fins to generate additional lateral force and change course [24]. In the turning test, the tail fin of HyperTuna swung to one side, with a large beat amplitude and a drive frequency of 2 Hz. Fig. 14(a) illustrates the whole turning process of HyperTuna at a phase difference of 200°. In this case, HyperTuna has a minimum turning radius of 0.47 BL, as shown in Fig. 14(b).

2. Diving–Floating Test

HyperTuna maintained neutral buoyancy at a drive frequency of 3 Hz in the test. As shown in Fig. 15, first, the pitch angle of the pectoral fins shifted to −45°, thus generating downward lift in the vertical direction and causing the body to dive. Then, it shifted to 45° to float. The body pitch angle of HyperTuna remained stable throughout the test.

3. Swimming in Open Water

To verify the practical operability and cruising ability of HyperTuna, we conducted swimming experiments in open water. The experimental site was Nan Lake, Nanguan District, Changchun. We traveled on an electric boat to track and control HyperTuna continuously throughout the journey, as shown in Figs. 16(a) and 16(b). The approximate trajectory of HyperTuna was recorded using the GPS of a smartphone, as shown in Fig. 16(c). HyperTuna swam approximately 800 m in 30 min, applying the optimized control parameter of 0.5 m/s. The total power consumption was approximately 9.1 Wh, measured through an on-board current sensor.

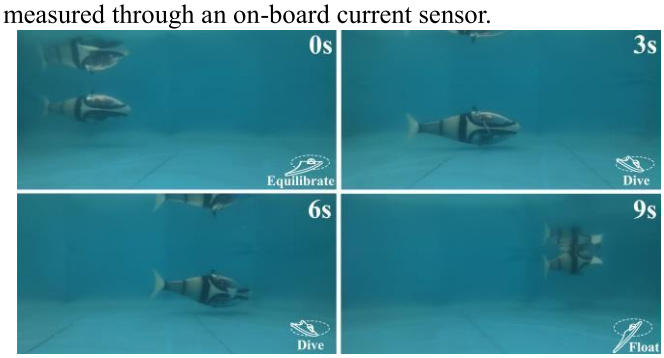

Fig. 15. Snapshots of diving–floating test.

Fig. 16. Swimming test in open water. (a)(b) Photo captured from boat. (c) Approximate trajectory of HyperTuna.

H. Discussion

HyperTuna has good programmability and swimming performance. The improvement in its performance, especially after optimization using the PSO algorithm, verifies the effectiveness of the established dynamic model and optimization algorithm. We summarize the key indicators of existing hydraulic soft robotic fish in Table V. Using the unified body-length unit to measure swimming speed is reasonable, although robotic fish have different appearances and body lengths. According to its comparison with similar hydraulic robotic fish, HyperTuna shows advantages in the number of joints, maximum frequency, swimming speed, and minimum turning radius. Compared with the bidirectional gear pumps used in previously reported robotic fish, the four-cylinder piston pump in HyperTuna has a higher driving frequency, resulting in faster swimming. HyperTuna also demonstrates excellent maneuverability, capable of performing turning and diving–floating motions. Therefore, the appearance of HyperTuna further raises the upper limit of the movement ability of hydraulic flexible robotic fish.

TABLE V
COMPARISON WITH EXISTING HYDRAULIC SOFT ROBOTIC FISH

Platform	Soft-bodied robot [41]	SoFi [21]	Collapsible robot [38]	Soft robot [39]	HyperTuna
Pressurized form	Gear pump	Gear pump	Gear pump	Gear pump	Piston pump
Soft actuator type	Hydraulic grid	Hydraulic grid	Collapsible	Hydraulic grid	Fiber constraint
Body length (m)	0.45	0.47	0.53	0.345	0.52
Number of joints	1	1	1	1	**2**
Maximum frequency (Hz)	1	1.4	0.75	0.67	**6**
Speed (BL/s)	0.23	0.51	0.5	0.5	**1.12**
Turning radius (BL)	No	1.66	No	No	**0.47**
Maneuver	Straight swimming	**3-D motion**	Straight swimming	Straight swimming	**3-D motion**

COT is a physical quantity that is easier to measure and is more accurate than swimming efficiency; however, it is often overlooked by researchers. Table VI lists COT reported for some typical soft robotic fish and real fish. HyperTuna is superior to most soft robots, but its COT is one order of magnitude higher than that of real fish. Therefore, HyperTuna may still be optimized in terms of driving methods and structural design to reduce COT.

TABLE VI
COT COMPARISON WITH EXISTING SOFT ROBOTIC FISH AND REAL FISH

Nonsmart material platform	COT (J/(kg*m))	Smart material platform	COT (J/(kg*m))
Wire-driven fish [18]	25.36	DEA robotic fish [42]	5621
Armed fish [43]	21.6	IPMC cownose ray [44]	2354
OCTOPUS [45]	17.7	DEA jellyfish [46]	340
Robotic octopus [47]	14.2	Real fish	COT (J/(kg*m))
Cyro [48]	10.9	Bluefin Tuna [49]	1.23
Multi-Flexible fish [5]	2.87	Yellow Tuna [50]	1.1
HyperTuna	12.1		

IV. CONCLUSION

Compared with single-joint robotic fish, multijoint structures create more flexible motion modes and more control parameters. However, designing multijoint structures is challenging, especially for hydraulically powered soft robotic fish. This paper introduces a hydraulically powered double-joint soft robotic fish. First, we propose a highly integrated hydraulic system in which a four-cylinder piston pump provides pressure pulses for the soft actuator. In addition to the external protective matrix and the internal drive units, soft bending sensors were installed in the neutral layer of the actuator to sense the fish swimming posture. Second, a theoretical deformation model and an FE model of the actuator were established to predict swimming performance. The calculated results agreed well with the experimental findings. Third, based on the hardware of HyperTuna, a PID–CPG controller was developed to control the swimming posture accurately. Fourth, considering the active soft tail, a Lagrange dynamic model combined with a multipseudolink method was established for HyperTuna. The hydrodynamic parameters of the model were obtained through a data-driven identification method. Based on the established model, the control parameters were optimized using a PSO algorithm. The experimental results showed that the maximum speed increased by 3.6% and COT decreased by up to 13.9% at 0.4 m/s after optimization. Consequently, the proposed robotic fish could achieve a maximum speed of 1.12 BL/s and a minimum COT of 12.1 J/(kg·m). Finally, 3-D swimming and field tests were conducted to verify its maneuverability and potential for practical application.

HyperTuna is a ‘fully-actuated’ robot fish (i.e., each joint can be controlled separately). The transmission loss of the four-cylinder piston pump and two drive joints is one of the important reasons that limit the COT of HyperTuna. In future work, we aim to make structural improvements to form an underactuated system to save energy. For example, the active Joint II may be converted into a passive joint with adjustable stiffness to reduce COT. In addition, we believe that adjusting the area or aspect ratio of the robotic fish tail fins online to increase its efficiency under different swimming conditions would be an interesting study.

APPENDIX

Supplementary Movie 1. Straight swimming test and comparison between experiment and simulation.

Supplementary Movie 2. Turning and diving–floating tests.

Supplementary Information: Manufacturing process of actuator, PCB design and Design of piston pump.

REFERENCES

[1] M. Sfakiotakis, D. M. Lane, and J. B. C. Davies, “Review of fish swimming modes for aquatic locomotion,” *IEEE J. Ocean. Eng.*, vol. 24, no. 2, pp. 237–252, Apr. 1999, doi: 10.1109/48.757275.

[2] G. V. Lauder and J. L. Tangorra, “Fish locomotion: biology and robotics of body and fin-based movements,” in *Robot Fish*, R. Du, Z. Li, K. Youcef-Toumi, and P. Valdivia Y Alvarado, Eds., in Springer Tracts in Mechanical Engineering., Berlin, Heidelberg: Springer Berlin Heidelberg, 2015, pp. 25–49. doi: 10.1007/978-3-662-46870-8_2.

[3] B. E. Flammang and G. V. Lauder, “Caudal fin shape modulation and control during acceleration, braking and backing maneuvers in bluegill sunfish, *Lepomis macrochirus*,” *J. Exp. Biol.*, vol. 212, no. 2, pp. 277–286, Jan. 2009, doi: 10.1242/jeb.021360.

[4] T. Desvignes, A. Carey, and J. H. Postlethwait, “Evolution of caudal fin ray development and caudal fin hypural diastema complex in spotted gar, teleosts, and other neopterygian fishes,” *Dev. Dyn.*, vol. 247, no. 6, pp. 832–853, Jun. 2018, doi: 10.1002/dvdy.24630.

[5] B. Lu, C. Zhou, J. Wang, Z. Zhang, and M. Tan, “Toward swimming speed optimization of a multi-flexible robotic fish with low cost of transport,” *IEEE Trans. Autom. Sci. Eng.*, pp. 1–12, 2023, doi: 10.1109/TASE.2023.3269775.

[6] R. J. Clapham and H. Hu, “iSplash-I: High performance swimming motion of a carangiform robotic fish with full-body coordination,” in *2014 IEEE International Conference on Robotics and Automation (ICRA)*, Hong Kong, China: IEEE, May 2014, pp. 322–327. doi: 10.1109/ICRA.2014.6906629.

[7] D. S. Barrett, M. S. Triantafyllou, D. K. P. Yue, M. A. Grosenbaugh, and M. J. Wolfgang, “Drag reduction in fish-like locomotion,” *J. Fluid Mech.*, vol. 392, pp. 183–212, Aug. 1999, doi: 10.1017/S0022112099005455.

[8] A. D. Marchese, C. D. Onal, and D. Rus, “Autonomous soft robotic fish capable of escape maneuvers using fluidic elastomer actuators,” *Soft Robot.*, vol. 1, no. 1, pp.

75–87, Mar. 2014, doi: 10.1089/soro.2013.0009.

[9] W. Zhou and Y. Li, "Modeling and analysis of soft pneumatic actuator with symmetrical chambers used for bionic robotic fish," *Soft Robot.*, vol. 7, no. 2, pp. 168–178, Apr. 2020, doi: 10.1089/soro.2018.0087.

[10] R. Wang, C. Zhang, Y. Zhang, W. Tan, W. Chen, and L. Liu, "Soft underwater swimming robots based on artificial muscle," *Adv. Mater. Technol.*, vol. 8, no. 4, p. 2200962, Feb. 2023, doi: 10.1002/admt.202200962.

[11] B. Mosadegh *et al.*, "Pneumatic networks for soft robotics that actuate rapidly," *Adv. Funct. Mater.*, vol. 24, no. 15, pp. 2163–2170, Apr. 2014, doi: 10.1002/adfm.201303288.

[12] K. Ning, P. Hartono, and H. Sawada, "Using inverse learning for controlling bionic robotic fish with SMA actuators," *MRS Adv.*, vol. 7, no. 30, pp. 649–655, Aug. 2022, doi: 10.1557/s43580-022-00328-w.

[13] T. Chen, O. R. Bilal, K. Shea, and C. Daraio, "Harnessing bistability for directional propulsion of soft, untethered robots," *Proc. Natl. Acad. Sci.*, vol. 115, no. 22, pp. 5698–5702, May 2018, doi: 10.1073/pnas.1800386115.

[14] G. Li *et al.*, "Self-powered soft robot in the Mariana Trench," *Nature*, vol. 591, no. 7848, pp. 66–71, Mar. 2021, doi: 10.1038/s41586-020-03153-z.

[15] T. Li *et al.*, "Fast-moving soft electronic fish," *Sci. Adv.*, vol. 3, no. 4, 2017, doi: 10.1126/sciadv.1602045.

[16] H. Li, M. Fan, Y. Yue, G. Hu, Q. He, and M. Yu, "Motion control of capsule-like underwater robot utilizing the swing properties of ionic polymer metal composite actuators," *J. Bionic Eng.*, vol. 17, no. 2, pp. 281–289, Mar. 2020, doi: 10.1007/s42235-020-0022-7.

[17] J. Shu *et al.*, "A liquid metal artificial muscle," *Adv. Mater.*, vol. 33, no. 43, p. 2103062, Oct. 2021, doi: 10.1002/adma.202103062.

[18] Y. Zhong, Z. Li, and R. Du, "A novel robot fish with wire-driven active body and compliant tail," *IEEEASME Trans. Mechatron.*, vol. 22, no. 4, pp. 1633–1643, Aug. 2017, doi: 10.1109/TMECH.2017.2712820.

[19] C. Qiu, Z. Wu, J. Wang, M. Tan, and J. Yu, "Locomotion optimization of a tendon-driven robotic fish with variable passive tail fin," *IEEE Trans. Ind. Electron.*, vol. 70, no. 5, pp. 4983–4992, May 2023, doi: 10.1109/TIE.2022.3189093.

[20] J. Qu *et al.*, "Recent advances on underwater soft robots," *Adv. Intell. Syst.*, p. 2300299, Oct. 2023, doi: 10.1002/aisy.202300299.

[21] R. K. Katzschmann, J. DelPreto, R. MacCurdy, and D. Rus, "Exploration of underwater life with an acoustically controlled soft robotic fish," *Sci. Robot.*, vol. 3, no. 16, p. eaar3449, Mar. 2018, doi: 10.1126/scirobotics.aar3449.

[22] J. Frame, N. Lopez, O. Curet, and E. D. Engeberg, "Thrust force characterization of free-swimming soft robotic jellyfish," *Bioinspir. Biomim.*, vol. 13, no. 6, p. 064001, Sep. 2018, doi: 10.1088/1748-3190/aadcb3.

[23] S. Liu, C. Liu, Y. Liang, L. Ren, and L. Ren, "Tunable stiffness caudal peduncle leads to higher swimming speed without extra energy," *IEEE Robot. Autom. Lett.*, vol. 8, no. 9, pp. 5886–5893, Sep. 2023, doi: 10.1109/LRA.2023.3300587.

[24] S. Du, Z. Wu, J. Wang, S. Qi, and J. Yu, "Design and control of a two-motor-actuated tuna-inspired robot system," *IEEE Trans. Syst. Man Cybern. Syst.*, vol. 51, no. 8, pp. 4670–4680, Aug. 2021, doi: 10.1109/TSMC.2019.2944786.

[25] H. F. Schulte, "The characteristics of the McKibben artificial muscle," 1961. [Online]. Available: https://api.semanticscholar.org/CorpusID:56578299

[26] E. Ball, Y. Lin, and E. Garcia, "Characterization and modeling of geometric variations in McKibben pneumatic artificial muscles," presented at the SPIE Smart Structures and Materials + Nondestructive Evaluation and Health Monitoring, R. J. Martín-Palma and A. Lakhtakia, Eds., San Diego, California, USA, Apr. 2013, p. 868605. doi: 10.1117/12.2009533.

[27] M. S. Triantafyllou, G. S. Triantafyllou, and D. K. P. Yue, "Hydrodynamics of fishlike swimming," *Annu. Rev. Fluid Mech.*, vol. 32, no. 1, pp. 33–53, Jan. 2000, doi: 10.1146/annurev.fluid.32.1.33.

[28] P. L. Nguyen, V. P. Do, and B. R. Lee, "Dynamic modeling of a non-uniform flexible tail for a robotic fish," *J. Bionic Eng.*, vol. 10, no. 2, pp. 201–209, Jun. 2013, doi: 10.1016/S1672-6529(13)60216-4.

[29] J. Wang, P. K. McKinley, and X. Tan, "Dynamic modeling of robotic fish with a base-actuated flexible tail," *J. Dyn. Syst. Meas. Control*, vol. 137, no. 1, p. 011004, Jan. 2015, doi: 10.1115/1.4028056.

[30] H.-J. Su, "A load independent pseudo-rigid-body 3R model for determining large deflection of beams in compliant mechanisms," in *Volume 2: 32nd Mechanisms and Robotics Conference, Parts A and B*, Brooklyn, New York, USA: ASMEDC, Jan. 2008, pp. 109–121. doi: 10.1115/DETC2008-49041.

[31] H.-J. Su, "A pseudorigid-body 3R model for determining large deflection of cantilever beams subject to tip loads," *J. Mech. Robot.*, vol. 1, no. 2, p. 021008, May 2009, doi: 10.1115/1.3046148.

[32] J. Zhu, C. White, D. K. Wainwright, V. Di Santo, G. V. Lauder, and H. Bart-Smith, "Tuna robotics: A high-frequency experimental platform exploring the performance space of swimming fishes," *Sci. Robot.*, vol. 4, no. 34, p. eaax4615, Sep. 2019, doi: 10.1126/scirobotics.aax4615.

[33] Z. Wang, L. Wang, T. Wang, and B. Zhang, "Research and experiments on electromagnetic-driven multi-joint bionic fish," *Robotica*, vol. 40, no. 3, pp. 720–746, Mar. 2022, doi: 10.1017/S0263574721000771.

[34] Q. Zhong *et al.*, "Tunable stiffness enables fast and efficient swimming in fish-like robots," *Sci. Robot.*, vol. 6, no. 57, p. eabe4088, Aug. 2021, doi: 10.1126/scirobotics.abe4088.

[35] R. Tong *et al.*, "Design and optimization of an untethered high-performance robotic tuna," *IEEEASME Trans. Mechatron.*, vol. 27, no. 5, pp. 4132–4142, Oct. 2022, doi: 10.1109/TMECH.2022.3150982.

[36] X. Liao, C. Zhou, Q. Zou, J. Wang, and B. Lu, "Dy-

namic modeling and performance analysis for a wire-driven elastic robotic fish," *IEEE Robot. Autom. Lett.*, vol. 7, no. 4, pp. 11174–11181, Oct. 2022, doi: 10.1109/LRA.2022.3197911.

[37] J. Yuan, J. Yu, Z. Wu, and M. Tan, "Enhancing swimming performance of a biomimetic robotic fish by optimizing oscillator phase differences of a CPG model," in *2015 IEEE International Conference on Robotics and Biomimetics (ROBIO)*, Zhuhai: IEEE, Dec. 2015, pp. 279–284. doi: 10.1109/ROBIO.2015.7418780.

[38] Q. Xia *et al.*, "Research on flexible collapsible fluid-driven bionic robotic fish," *Ocean Eng.*, vol. 276, p. 114203, May 2023, doi: 10.1016/j.oceaneng.2023.114203.

[39] G. Chen, X. Yang, Y. Xu, Y. Lu, and H. Hu, "Neural network-based motion modeling and control of water-actuated soft robotic fish," *Smart Mater. Struct.*, vol. 32, no. 1, p. 015004, Jan. 2023, doi: 10.1088/1361-665X/aca456.

[40] M. Wang, X. Li, H. Dong, and S. Yang, "A PSO-based CPG model parameter optimization method for biomimetic robotic fish," in *2017 Chinese Automation Congress (CAC)*, Jinan: IEEE, Oct. 2017, pp. 3445–3449. doi: 10.1109/CAC.2017.8243376.

[41] R. K. Katzschmann, A. D. Marchese, and D. Rus, "Hydraulic autonomous soft robotic fish for 3D swimming," in *Experimental Robotics*, vol. 109, M. A. Hsieh, O. Khatib, and V. Kumar, Eds., in Springer Tracts in Advanced Robotics, vol. 109. , Cham: Springer International Publishing, 2016, pp. 405–420. doi: 10.1007/978-3-319-23778-7_27.

[42] J. Shintake, V. Cacucciolo, H. Shea, and D. Floreano, "Soft biomimetic fish robot made of dielectric elastomer actuators," *Soft Robot.*, vol. 5, no. 4, pp. 466–474, Aug. 2018, doi: 10.1089/soro.2017.0062.

[43] T. Paschal, J. Shintake, S. Mintchev, and D. Floreano, "Development of bio-inspired underwater robot with adaptive morphology capable of multiple swimming modes," in *2017 IEEE/RSJ International Conference on Intelligent Robots and Systems (IROS)*, Vancouver, BC: IEEE, Sep. 2017, pp. 4197–4202. doi: 10.1109/IROS.2017.8206281.

[44] V. Sunkara, Z. Ye, A. Chakravarthy, and Z. Chen, "Collision avoidance by IPMC actuated robotic fish using the collision cone approach," in *2016 IEEE International Conference on Simulation, Modeling, and Programming for Autonomous Robots (SIMPAR)*, San Francisco, CA, USA: IEEE, Dec. 2016, pp. 238–245. doi: 10.1109/SIMPAR.2016.7862402.

[45] M. Cianchetti, M. Calisti, L. Margheri, M. Kuba, and C. Laschi, "Bioinspired locomotion and grasping in water: the soft eight-arm OCTOPUS robot," *Bioinspir. Biomim.*, vol. 10, no. 3, p. 035003, May 2015, doi: 10.1088/1748-3190/10/3/035003.

[46] C. Christianson *et al.*, "Jellyfish-inspired soft robot driven by fluid electrode dielectric organic robotic actuators," *Front. Robot. AI*, vol. 6, p. 126, Nov. 2019, doi: 10.3389/frobt.2019.00126.

[47] M. Sfakiotakis, A. Kazakidi, and D. P. Tsakiris, "Octopus-inspired multi-arm robotic swimming," *Bioinspir. Biomim.*, vol. 10, no. 3, p. 035005, May 2015, doi: 10.1088/1748-3190/10/3/035005.

[48] A. A. Villanueva, K. J. Marut, T. Michael, and S. Priya, "Biomimetic autonomous robot inspired by the *Cyanea capillata* (Cyro)," *Bioinspir. Biomim.*, vol. 8, no. 4, p. 046005, Oct. 2013, doi: 10.1088/1748-3182/8/4/046005.

[49] J. M. Blank, C. J. Farwell, J. M. Morrissette, R. J. Schallert, and B. A. Block, "Influence of swimming speed on metabolic rates of juvenile pacific bluefin tuna and yellowfin tuna," *Physiol. Biochem. Zool.*, vol. 80, no. 2, pp. 167–177, Mar. 2007, doi: 10.1086/510637.

[50] V. Di Santo, C. P. Kenaley, and G. V. Lauder, "High postural costs and anaerobic metabolism during swimming support the hypothesis of a U-shaped metabolism–speed curve in fishes," *Proc. Natl. Acad. Sci.*, vol. 114, no. 49, pp. 13048–13053, Dec. 2017, doi: 10.1073/pnas.1715141114.

Sijia Liu received the B.Eng. degree in Mechanical Engineering from Jilin University, Changchun, China, in 2019.

He is currently working toward the Ph.D. degree with the School of Mechanical Science and Aerospace Engineering, Jilin University, Changchun, China. His research focuses on bionic hydraulic drive technology of soft robotic fish, with a focus on reducing energy consumption of the robots.

Chunbao Liu received the M.S. and Ph.D. degree from School of Mechanical and Aerospace Engineering, Jilin University in 2006 and 2009 respectively, majored in Mechanical design and theory.

He is a professor of the School of Mechanical Science and Aerospace Engineering at Jilin University. He researches in the field of fluid and micro-fluidic simulation, soft actuator and robotics, and mechanical engineering. He presided over and participated in more than 20 national, provincial and ministerial projects and has over 50 research papers.

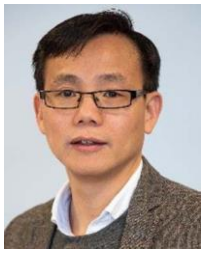

Guowu Wei (Member, IEEE) received the Ph.D. degree in robotics from King's College London, London, U.K., in 2012.

He is currently a Lecturer of Robotics and Mechanical Engineering with the School of Science, Engineering and Environment, University of Salford, Salford, U.K. He has more than 140 peer-reviewed publications. His research was funded by EPSRC, EU-FP7, ICUK, NSFC, and Royal Academy of Egineering. His research interests include robotics, mechatronics, manipulation and grasping, reconfigurable mechanisms and robotics, and bioro-

botics.

Dr. Wei is the Associate Editor for *Robotica* and *Journal of Mechanical Engineering Science*, the Topic Editor for *Mechanical Science*, the Academic Editor for *Applied Bionics and Biomechanics*, and the Associate Editor for the IEEE/RSJ International Conference on Intelligent Robots and Systems and IEEE International Conference on Robotics and Automation. He is currently the Deputy Chair of IFToMM MO U.K.

Luquan Ren is an academician at the Chinese Academy of Sciences. He obtained his M.A. degree from Jilin University of Technology in 1981.

He became a professor and a doctoral supervisor in 1991 and 1993, respectively. He is engaged in research and education of bionic science and engineering and ground mechanical engineering. He is the academic leader of the agricultural mechanization engineering national key disciplines and bionic science and engineering doctoral program of Jilin University.

Lei Ren (Member, IEEE) received the Ph.D. degree in biomechanical engineering from the University of Salford, Manchester, U.K., in 2005.

He is currently the Leader of biomechanics specialism with Department of Mechanical, Aerospace, and Civil Engineering, University of Manchester and with the Key Laboratory of Bionic Engineering, Ministry of Education, Jilin University, Changchun, China.

Dr. Ren is currently the Deputy General Secretary of the International Society of Bionic Engineering, Nottingham, U.K. and with the Council of Chairs, Biomedical Engineering Society, Landover, MD, USA. His research interests include the field of biorobotics and biomechanics, including humanoid locomotion, hand grasping and manipulation, and bioinspired limb prosthetics. His research works have been reported by Nature, Science News, Wired, Telegraph, Science Daily, and BBC.